JOURNAL OF MATERIALS SCIENCE **39** (2004) 5987–5994

Crystallographic characterization and indentation mechanical properties of LaB_6-ZrB_2 directionally solidified eutectics

H. DENG, E. C. DICKEY*
Department of Materials Science and Engineering and The Materials Research Institute, The Pennsylvania State University, 248 MRL, University Park, PA 16802, USA
E-mail: ecd10@psu.edu

Y. PADERNO, V. PADERNO, V. FILIPPOV
The Institute for Problems of Materials Sciences of Academy of Sciences of Ukraine, 3, Krzhyzhanovsky Str., 252142 Kiev, Ukraine

A. SAYIR
NASA Lewis Research Center, 21000 Brookpark Road, Cleveland, OH 44135, USA

LaB_6-ZrB_2 eutectics were directionally solidified by a zone melting process. The microstructure and crystallography were characterized by X-ray diffraction, optical microscopy and transmission electron microscopy. The anisotropies of hardness and indentation fracture toughness were assessed by making measurements along different crystallographic directions on both transverse and longitudinal sections. While the hardness did not vary appreciably between the two orientations, the fracture toughness was observed to be highly anisotropic. Toughening behavior was observed on longitudinal sections with crack deflection and bridging mechanisms apparent. Cracks were difficult to initiate on transverse sections along directions perpendicular to the growth direction, but for 20 N loads an indentation fracture toughness of 11 MPa$\sqrt{m}$ could be measured.

© *2004 Kluwer Academic Publishers*

1. Introduction

Ceramic directionally solidified eutectics (DSEs) have attracted considerable attention because of their thermodynamic compatibility and microstructural stability up to the eutectic invariant point [1]. Oxide DSEs have received the most recent attention because they have demonstrated excellent strength and creep resistance up to high-temperatures (>1200°C), which makes them attractive as high-temperature structural materials [2–4]. For example, Al_2O_3-$ZrO_2(Y_2O_3)$ maintains about 70% of its strength up to 1400°C [4] and has a deformation rate less than 1/10 of off-*c*-axis single crystalline sapphire [3]. One limiting property of this class of materials, however, may be the low fracture toughness because the interfaces between the two phases typically adopt low-energy orientation relationships during the directional solidification process, which promotes strong bonding and prevents interface debonding [5]. On the other hand, while boride DSEs have received relatively less attention, there are indications that these materials may have some advantageous mechanical properties in comparison to their oxide counterparts.

In general, borides of rare-earth and d-transitional metals have outstanding refractory properties with high hardness, high chemical stability and ultra-high melting points that usually range between 2300–3200°C. LaB_6-ZrB_2 DSEs, which have a eutectic temperature of 2442 ± 40°C, exhibit high bend strength (1000–1320 MPa) and excellent thermal shock resistance (500 K/min) [6]. Fracture toughness has been investigated in LaB_6-ZrB_2 DSEs using conventional, macroscopic 3-point bend and Vickers micro-indentation methods. In the conventional tests, LaB_6-ZrB_2 DSEs showed exceptionally high fracture toughness (16.3–27.8 MPa$\sqrt{m}$ [6] or 17.8 MPa$\sqrt{m}$ [7]) when the initial notches were cut perpendicular to the rod axis. The Vickers indentation method was also utilized by Chen *et al.* to measure fracture toughness [7]. They performed tests on planes parallel and perpendicular to the rod axis, and quantified the fracture toughness as 8.2 and 8.7 MPa$\sqrt{m}$, respectively.

This study aims to build upon earlier studies [6–9] and to thoroughly characterize the microstructure, crystallography and interface structure of LaB_6-ZrB_2 DSEs. In addition, the work aims to measure the anisotropy of hardness and fracture toughness and to identify toughening mechanisms in the material, which may also be highly anisotropic.

2. Experimental procedure

2.1. *Crystallographic characterization*

LaB_6-ZrB_2 eutectics were directionally solidified by a zone melting process as described in detail elsewhere [6]. The eutectic rod was grown at a rate of 6.0 mm/min in a 0.3 MPa argon atmosphere, and the final rod was 6 mm in diameter.

To investigate the microstructure, transverse (perpendicular to the growth direction) and longitudinal (parallel to the growth direction) sections of the rod were cut with a low-speed diamond saw, polished with diamond-embedded paper and imaged by optical microscopy. X-ray diffraction pole figure analysis on transverse sections was used to examine the crystallographic texture.

In order to observe the crystallographic orientation relationship between the LaB_6 and ZrB_2 phases, conventional TEM imaging and diffraction were performed on both transverse and longitudinal sections. To facilitate high-resolution imaging, the specimens were oriented by Laué diffraction such that the surface normal was parallel to [001]-LaB_6 for "transverse" sections, although it should be noted that this was 30° away from the growth axis. Longitudinal TEM sections were prepared with the sample normal being approximately along $[\bar{1}2\bar{1}0]$ -ZrB_2. Specimens with dimensions of 3×3 mm^2 were cut from the center of the eutectic rod and mechanically thinned and polished by lapping with diamond-embedded paper on both sides to a thickness of 2–4 μm. A Fishione ion mill was utilized to perforate the specimens with 5.0 kV Ar ions at a 15° inclination to the specimen surface. Specimens were finally thinned to electron transparency and cleaned by the ion beam with 4.0 kV Ar ions at an 8° inclination angle. Conventional TEM experiments were performed on a Philips 420 TEM outfitted with a W-filament gun and operated at 120 kV. Standard bright field (BF) images, convergent beam electron diffraction and selected area diffraction (SAD) patterns were taken for microstructural and crystallographic characterization. High-resolution TEM (HRTEM) images were acquired on a JEOL 2010F field-emission gun TEM operated at 200 kV.

2.2. *Mechanical properties measurements*

Hardness and fracture toughness were measured on the transverse and longitudinal sections at room temperature. Because the amount of material was not large enough for conventional, macroscopic fracture toughness tests, the Vickers indentation method was employed. The fracture toughness, K_{IC}, was calculated from the length, c, of the indentation-induced cracks by following equation [10]:

$$K_{Ic} = \delta \times \left(\frac{E}{H}\right)^{\frac{1}{2}} \times \left(\frac{P}{c^{3/2}}\right) \qquad (1)$$

where δ is an indenter constant that equals to 0.016 for Vickers indenter, E is the Young's Modulus and H is the hardness. The crack length, c, was defined as the distance from the center of the indentation to the tip of the crack, as measured from SEM and optical microscopy images. The modulus-to-hardness ratio (*E/H*) is microstructure-dependent and was expected to be anisotropic in these materials. Hence, it was experimentally measured by a Knoop indentation method which utilized the fact that elastic recovery changes the ratio of the major to minor indentation lengths relative to that of the indenter [11] as per Equation 2:

$$\frac{b}{a} \approx \frac{b}{a'} = \frac{b'}{a'} - \left(\frac{\alpha H}{E}\right) \qquad (2)$$

where a and b are the measured major and minor diagonals of the indentation, a' and b' are the major and minor diagonals of the Knoop indenter ($b'/a' = 0.14$) and α is a constant equal to 0.45. The lengths of the indentation diagonals were determined from optical micrographs.

The indentations for hardness and fracture toughness measurements were made by a microhardness tester (LECO V-100-C1) outfitted with Vickers and Knoop indenters. Measurements were made with various loadings from 2 to 20 N. All testing was performed on the central area of the bulk sample to avoid effects from microstructural variations, which were present near the edges. Six indentations were made for each loading from which a standard deviation on the measurement was calculated. In order to prevent influences from surface residual stresses and possible surface relief, all specimens were carefully polished by diamond lapping paper and finally by colloidal silica before indentation.

3. Results and discussion

3.1. *Microstructure*

The bulk LaB_6-ZrB_2 DSE was a dark purple rod about 6 mm in diameter. Optical micrographs of the transverse section (Fig. 1), showed that the growth of ZrB_2 fibers (white phase) was uniform at the center of the rod (c), non-uniform at the edge (a), and were separated by several concentric circular matrix belts around the center (b). In the center or homogeneous area, the average diameter of fibers was 0.6 μm. The volume fraction of the ZrB_2 phase was 18% as calculated by area fractions from digital micrographs taken from a transverse section at the center of the specimen (e.g., Fig. 1c); this coincides closely with that expected from the eutectic composition—17% [12].

The optical micrographs of the longitudinal section (Fig. 2c), illustrated that the ZrB_2 fibers were uniformly distributed in the matrix and parallel to each other. It was also apparent that the fiber diameters did not change appreciably along their growth direction. Since the longitudinal section was not cut perfectly parallel to the growth direction, only a portion of the fiber was visible and had an average length of at least 60 μm, which implied that the total length of the fiber was even longer. Pores evident in the images resulted from spallation during sample preparation, indicative of the weak bonding between the fibers and matrix. Fig. 2b showed that some banding occurred along the growth axis.

Based on the results shown in Fig. 1, the LaB_6 solidified as a primary phase in the outer regions due to

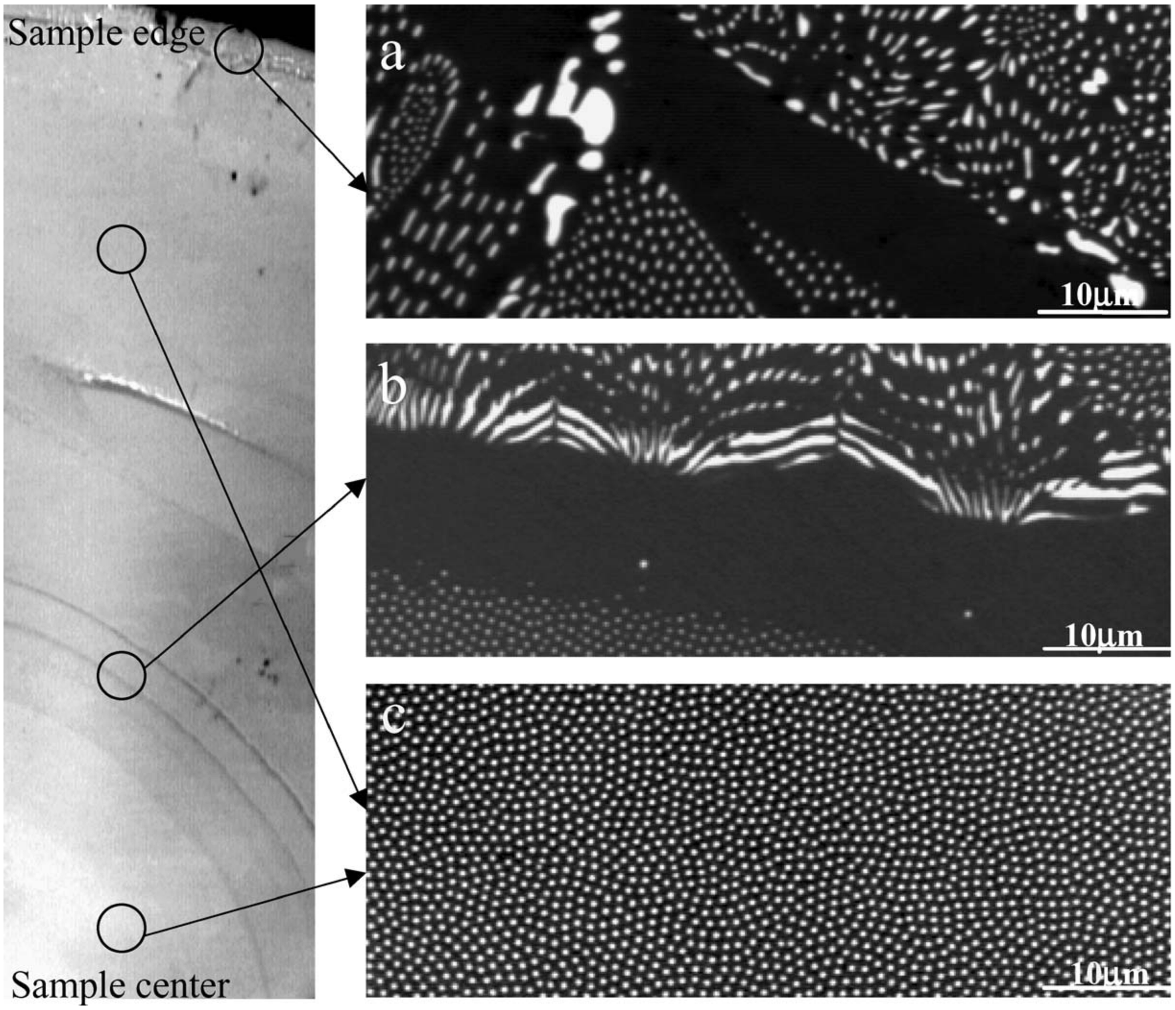

Figure 1 Optical microscopy images of LaB_6-ZrB_2 DSE. The growth of ZrB_2 fibers (white phase) is uniform at the center of the rod (c), non-uniform at the edge (a), and separated by several concentric circular matrix belts around the center (b).

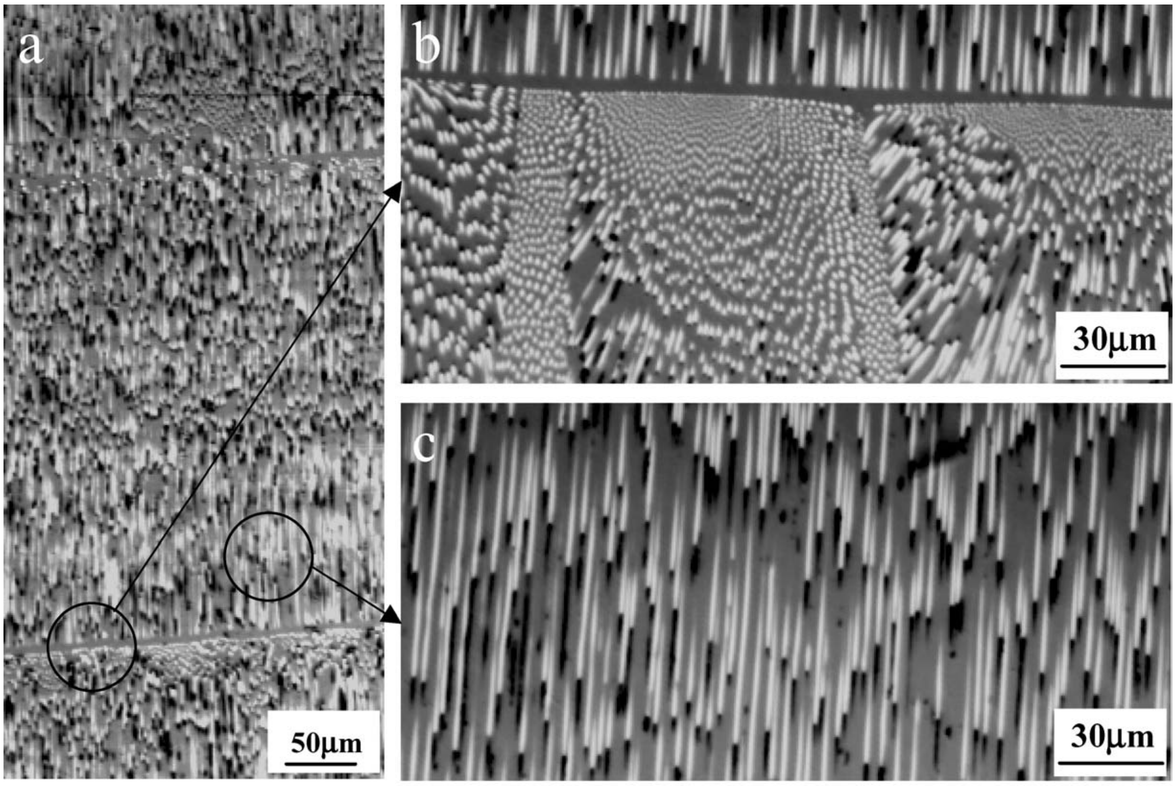

Figure 2 Optical micrographs of the longitudinal section illustrates that the ZrB_2 fibers are uniformly distributed in the matrix and parallel to each other.

the larger temperature gradient at the surface of the rod. This primary LaB_6 phase solidification shifted the composition off of the eutectic, which had to be compensated by changing the volume fraction of both phases. From a solidification point of view, these radial bands are similar to colony structures. Banded regions are usually convex toward the liquid, and the curvature is greater at the sides than at the center. The liquid-solid interface had greater curvature at the edges because at this location heat was extracted by the surrounding and the thermal gradient was larger. Fig. 2a showed that the bands of LaB_6 were not parallel to each other. This contradicts the notion that the banding was associated with the undercooling of the solid-liquid front [13, 14]. Additionally, optical microscopy analysis (Figs 1 and 2) indicated that the banding is severe. The ZrB_2 phase ceased to grow in regions and the LaB_6 phase grew laterally as shown in Fig. 1b. Rods of ZrB_2 terminated suddenly and were enveloped by the LaB_2. These observations suggest that the type of banding observed in this system is very strong and cannot be explained by constitutional undercooling alone. In oxide DSEs, a gradual transition from pronounced colony structure to faulted parallel lamellar (or rods) has been noticed [3, 15]. This behavior was nothing more than a subtle change in lamellar spacing caused by the formation of a few extra lamellae during solidification and did not affect the tensile strength of the oxide DSEs [3]. In contrast to oxide DSEs, the severe banding observed in the LaB_6-ZrB_2 eutectic was most likely associated with thermal instabilities, presumably due to variation in the power to the induction coil, but confirmation will require further study. It is, however, important to point out that the severe banding may have a strong effect on the overall tensile strength of the specimen.

3.2. *Crystallographic characterization*

The X-ray pole figures (Fig. 3) from the transverse section showed that the angle between the growth direction and the [001] axis of LaB_6 was 29° and the [0001] axis of ZrB_2 was 25°. Fig. 3 also indicates that two subgrains of the LaB_6 matrix were present within the diffraction volume. The angles between the two subgrains were approximately 18°. Previous studies have reported the growth axes to be along [001], although explicit pole figure analysis was not performed [16, 17]. The possible contradiction may be that in the present work, unlike previous studies [16, 17], the initial melted zone was maintained for several minutes before solidification for better homogenization. The role of the seed crystal in this case was fully excluded and the crystallization was homogeneous.

The TEM observations from the transverse-section specimens are summarized in Fig. 4. Fig. 4g is a SAD pattern, which confirms previous data [16] that the [0001]-ZrB_2 was nominally parallel to the [001]-LaB_6 and (110)-LaB_6 paralleled (1$\bar{1}$00)-ZrB_2. The intensity distributions apparent in Fig. 4c show that there was actually a 2.0° mistilt between the two [001] axes along the [5$\bar{2}$0]-LaB_6 direction. Furthermore, electron diffraction patterns a, b, e, f indicated that all of the fibers within the local area were oriented nominally the same with only about 0.02° deviation between the c-axes of different fibers. This result implies that the ZrB_2 phase was locally single crystalline in a 10 μm^2 area. Fig. 5 is a HRTEM micrograph taken along the [001]-LaB_6 zone axis, which shows a clean interface lacking any amorphous phase between the fiber and matrix.

The TEM results of the longitudinal section specimen are shown in Fig. 6. Fig. 6a is a low magnification bright-field TEM image, which shows that the fibers were distributed uniformly in the LaB_6 matrix. The angle between adjacent fibers was about 1.6°, which indicates that all fibers grew almost parallel to each other. Note that this mistilt is larger than that observed from adjacent fibers in the transverse sections, and may indicate that the crystallographic texture varied along the specimen length. Fig. 6c is the SAD pattern taken from two adjacent phases. The angles between the fiber axis and the c-axes of LaB_6 and ZrB_2 were 34.5° and 27.0° respectively. A mistilt between the c-axes by 7.5° was also evident, which was larger than the result from the transverse specimen in Fig. 4. Since transverse and longitudinal specimens were prepared from different

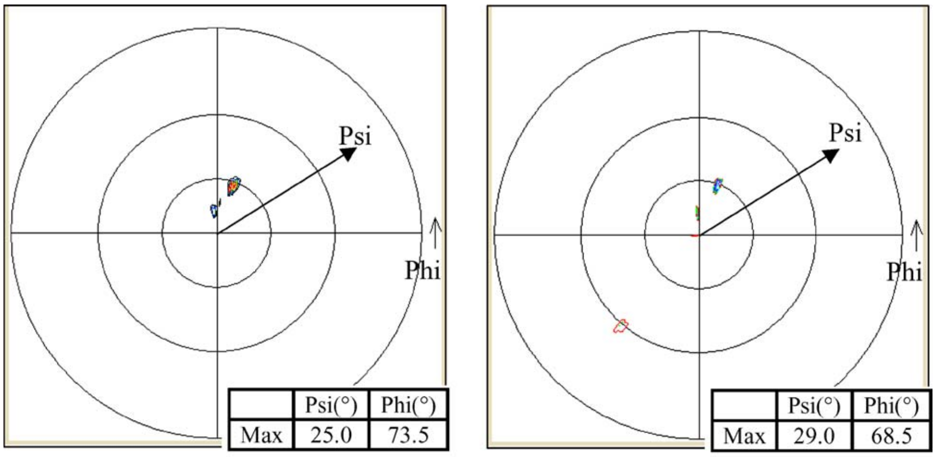

Pole figure of ZrB_2(0001) in LaB_6-ZrB_2

Pole figure of LaB_6(001)in LaB_6-ZrB_2

Figure 3 X-ray pole figures from the transverse section shows that the angles between the growth direction (located at 0° Psi) and the c-axes are 29° for LaB_6 and 25° for ZrB_2.

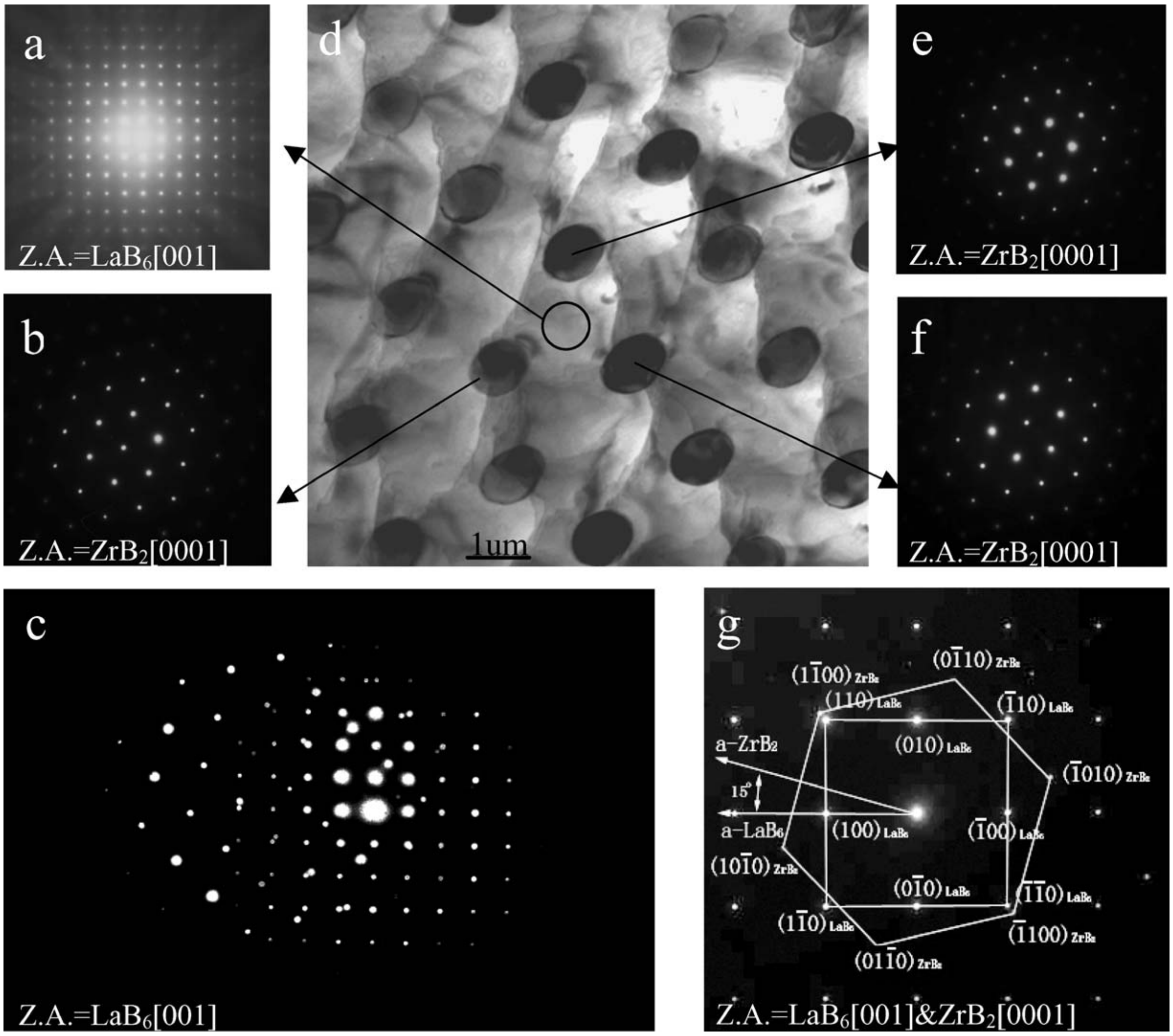

Figure 4 TEM data from the transverse section of a LaB_6-ZrB_2 DSE. g is the SAD pattern, which illustrates that the [0001] ZrB_2 is approximately parallel to [0001] LaB_6 and (110) LaB_6 parallels (1$\bar{1}$00) ZrB_2. Kikuchi lines evident in (c) show that there is actually a small misorientation between the two phases. Electron diffraction patterns from individual fibers (b, e, f) indicate that all of the LaB_6 fibers are locally oriented in the same direction within 0.02 degrees.

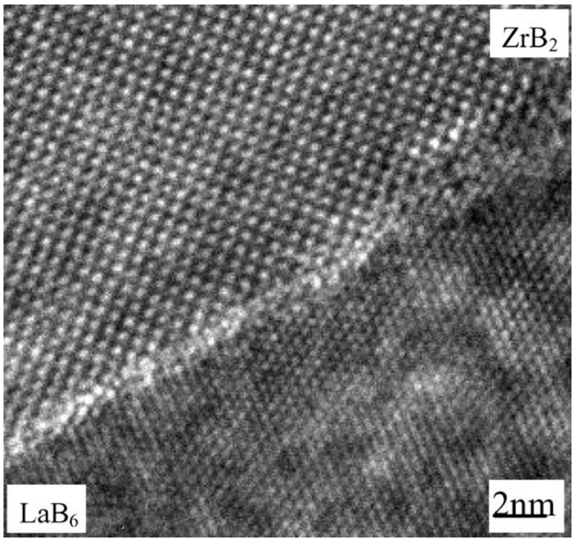

Figure 5 HRTEM micrograph along the [001] LaB_6 zone axis shows a clean and abrupt interface between the fiber and matrix.

parts of the eutectic rod, the mistilt dissimilarity indicates a positional dependence of the orientation. These findings are inconsistent with previous reports that showed the c-axes to be parallel to the fiber axis. As discussed above, it is possible that the crystallographic orientation may depend sensitively on exact growth conditions.

3.3. *Mechanical properties*

Table I summarizes the hardness and fracture toughness results. Error bars were calculated from the standard deviation of six measurements. Back-reflection Laué patterns indicated that the transverse section was parallel to the (023) plane of LaB_6, which was about 34° away from the (001) plane of LaB_6. Indentations were oriented so that their diagonals were parallel to [100]-LaB_6 and [03$\bar{2}$]-LaB_6. Within the error, the

TABLE I Hardness and fracture toughness of LaB_6-ZrB_2 as measured from Vickers indentation

	Transverse section		Longitudinal section	
	$[100]_{LaB_6}$	$[03\bar{2}]_{LaB_6}$	$[\bar{2}13]_{LaB_6}$	$[4\bar{2}3]_{LaB_6}$
Fracture toughness (MPa$\sqrt{m}$)	4.6 ± 0.3	4.2 ± 0.8	3.5 ± 0.7	11.1 ± 1.1
Hardness (GPa)	22.6 ± 0.7		21.7 ± 0.6	

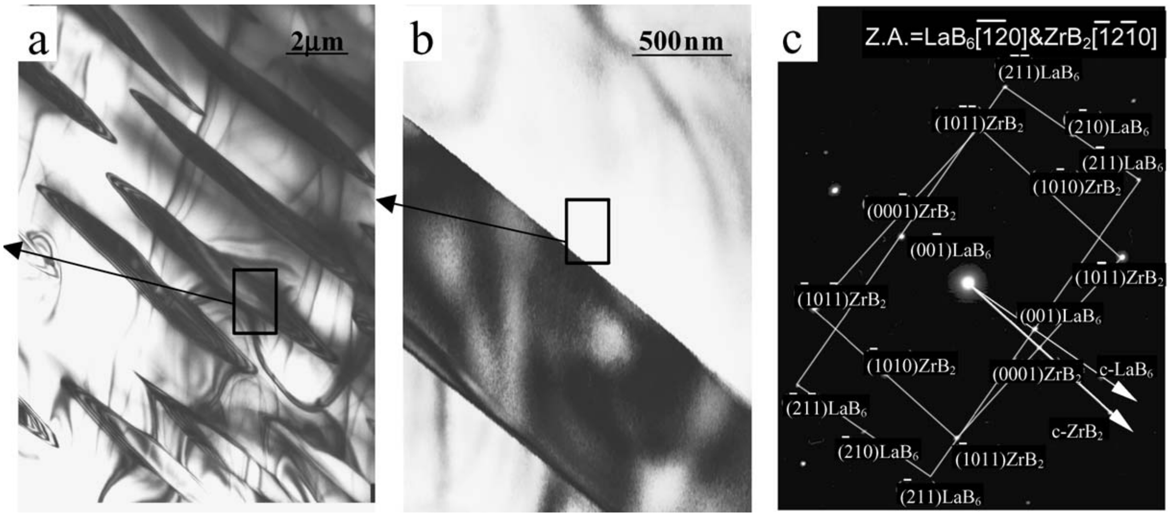

Figure 6 TEM data from the longitudinal section specimen. (a) is a low magnification bright-field image showing that the fibers are distributed uniformly in the LaB_6 matrix. The angle between adjacent fibers is about 2°. (c) is the SAD pattern taken from a phase boundary in (b). The angles between the fiber axis and the *c*-axes of LaB_6 and ZrB_2 are 34.5° and 27.0° respectively.

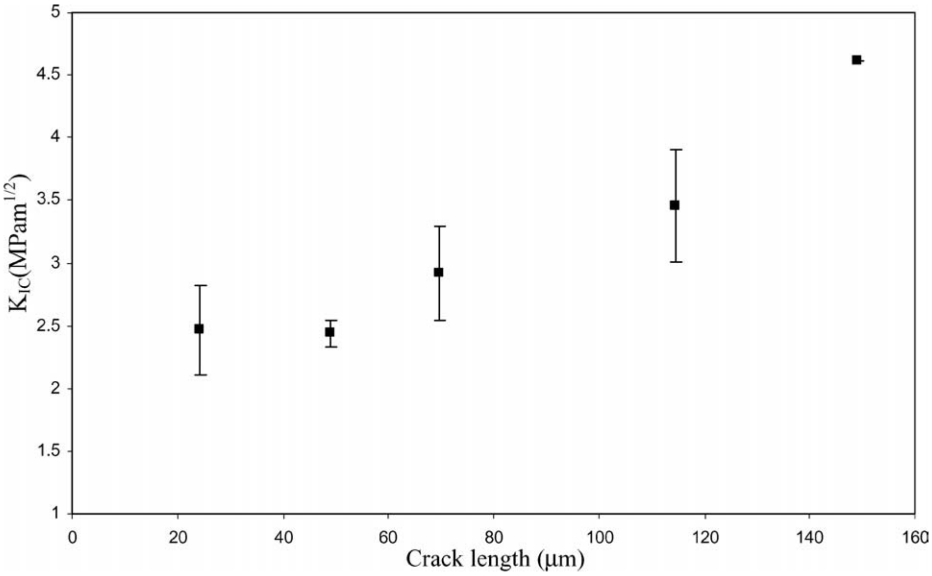

Figure 7 The fracture toughness versus crack-length curve from indentations made on transverse sections.

fracture toughness was the same along these two crystallographic directions— ∼4 MPa$\sqrt{m}$. Fig. 7 shows the fracture toughness versus crack length curve from indentations made on the transverse plane. We expected the fracture toughness to be relatively low in this orientation since the only toughening mechanism that could be operative in this orientation is crack deflection, while a bridging mechanism would not possible. Indeed, SEM

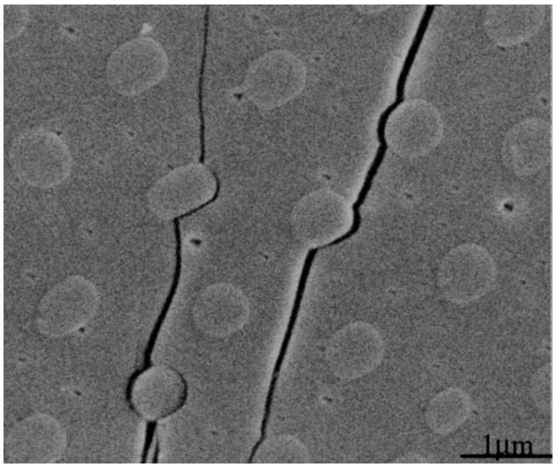

Figure 8 SEM image of a crack on the transverse section.

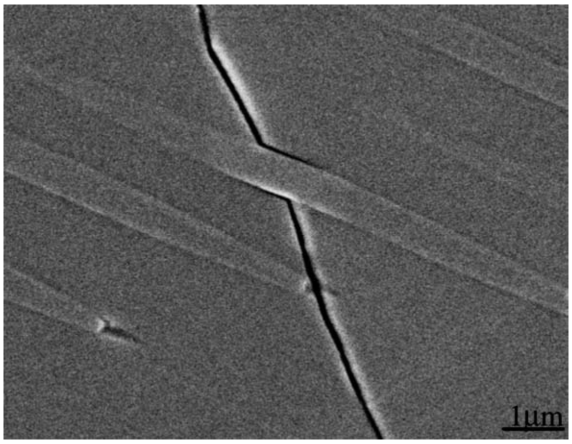

Figure 9 SEM image of a crack on the longitudinal section.

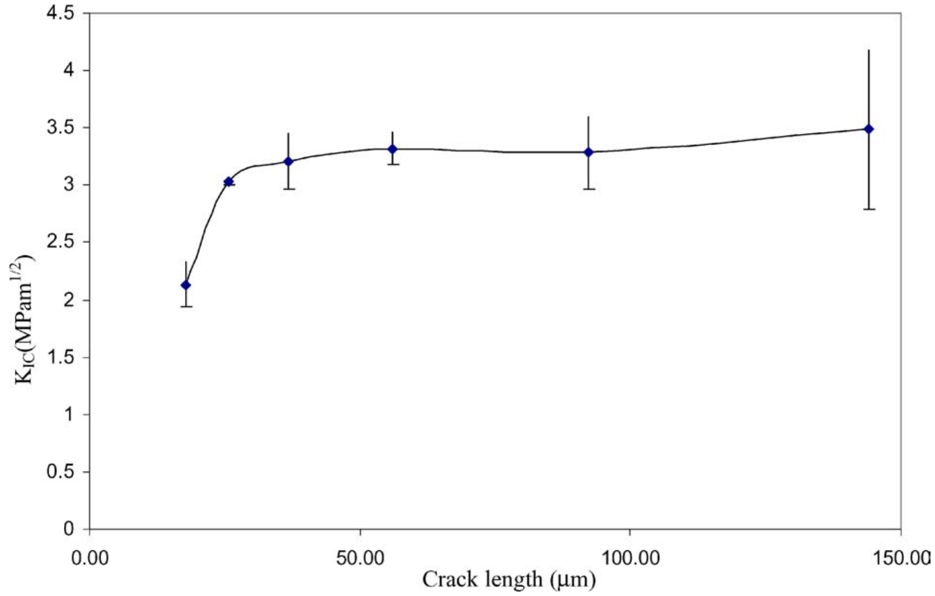

Figure 10 The fracture toughness versus crack-length curve of the longitudinal section.

images of cracks propagating on the transverse section (Fig. 8), indicate that the cracks debonded the fiber-matrix interface.

Indentation fracture toughness was also measured on longitudinal sections corresponding to the $(\bar{1}\bar{2}0)$ plane of LaB_6. Indentations were oriented so that the indenter diagonals were placed along the $[\bar{2}13]$-LaB_6 and $[4\bar{2}3]$-LaB_6 directions, almost parallel or perpendicular to the fibers, respectively. As shown in Fig. 9, interface debonding and subsequent crack bridging was clear for cracks initiated near the $[\bar{2}13]$-LaB_6 direction. As shown in Fig. 10, a maximum fracture toughness of 3.5 MPa$\sqrt{m}$ was measured.

On the longitudinal sections, the fracture toughness was very anisotropic and it was very difficult to initiate cracks along the $[4\bar{2}3]$-LaB_6 direction, which was approximately normal to the fiber axes. There were no obvious cracks perpendicular to the fiber up to 10 N indentation loads, as shown in Fig. 11. Cracks initiated with 20 N loading were used for the fracture toughness calculations, the results of which are summarized in Table I. The measured fracture toughness of 11 MPa$\sqrt{m}$ was roughly 3 to 4 times higher than the fracture toughness measured along the other specimen directions.

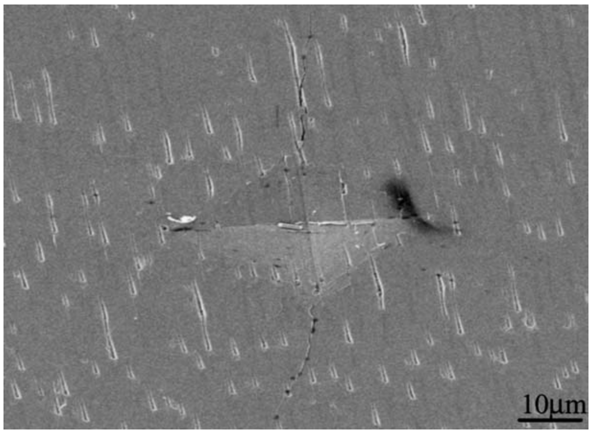

Figure 11 SEM image of indentation-induced cracks on a longitudinal section. While cracks are easily initiated parallel to the fibers, almost no cracks are initiated perpendicular to the fibers up to 10 N.

There are some quantitative differences between our fracture toughness measurements and those reported earlier in the literature [6, 7]. Chen's group also used the indentation method on transverse and longitudinal sections and reported values of 8.7 and 8.2MPa$\sqrt{m}$, respectively. There are two possible reasons for the differences. Firstly, although both groups investigated "transverse" and "longitudinal" sections, the crystallographic orientations were different because of the different growth axes. Also the crack propagation directions of previous studies were not reported, but as shown in the present study, the fracture toughness was highly orientation dependent.

Previous three-point-bend measurements performed with the crack initiated normal to the fiber axes yielded fracture toughnesses of 16.3–27.8 MPa$\sqrt{m}$ [6] and 17.8 MPa$\sqrt{m}$ [7], significantly higher than those reported here. The discrepancies were most likely due to the fundamental limitations of the indentation-based measurements. In Equation 1, the 3 parameters that affect the indentation fracture toughness value are δ, (E/H) and c. δ is a constant which depends on the deformation geometry, i.e., the crack model. The value utilized for measurements was based on the radial crack in isotropic materials. However, usually lateral cracks, spreading beneath the indentation surface, are generated during the final part of the indentation loading procedure [18], interact with radial cracks, and then cause surface chipping. In this case, "0.016" is not valid any more and the crack length c may be overestimated because of the surface chipping. Equation 1 also illustrates that c is the most significant parameter affecting the K_{IC}. To decrease the error associated with this parameter, firstly, a well polished surface and good micrographs are required to determine the crack tip. Secondly, and more important in practice, it is better to use long enough cracks to avoid effects from microstructural inhomogeneity.

Unfortunately, the typical c is about 100 μm, which means a 1 μm defect is big enough to introduce significant error into the equation. Moreover, the indentation-induced cracks may not have been long enough to fully realize the bridging forces from the intact fibers in the crack wake and certainly the fiber-pullout mechanism could not have been operative in these tests. Although the indentation tests had these limits, the indentation method was still useful for evaluating relative properties in a specimen that was not amenable to macroscopic testing. Certainly, more comprehensive and accurate macroscopic bend tests (e.g., ASTM C14-21) are warranted to quantify the true fracture toughness of this material.

4. Conclusions

A variety of diffraction and imaging techniques were used to characterize the microstructure and crystallography of $\mathrm{LaB_6}$-$\mathrm{ZrB_2}$ directionally solidified eutectics. It was observed that the $\mathrm{ZrB_2}$ fibers grew uniformly in the $\mathrm{LaB_6}$ matrix and were parallel to each other. For samples grown at 6.0 mm/min, the average diameter of the fibers was 0.6 μm and the average length was longer than 60 μm. The orientation relationship between the two phases was nominally:

$$[001]\ \mathrm{LaB_6}\text{-}//[0001]\text{-}\mathrm{ZrB_2}$$

$$(110)\ \mathrm{LaB_6}//(1\bar{1}00)\mathrm{ZrB_2}$$

which was consistent with previous reports [17, 19]. However, we observed about a 7° mistilt between the c-axes of the two phases. The $\mathrm{LaB_6}$-$\mathrm{ZrB_2}$ DSE had high hardness at room temperature—22.6 ± 0.7 and 21.7 ± 0.6 on the transverse and longitudinal planes, respectively. The indentation-induced crack propagation resistance was strongly anisotropic with the highest fracture toughness along the direction perpendicular to fibers (11 MPa$\sqrt{m}$) . The dominant toughening mechanisms along this section were crack deflection and crack bridging.

Acknowledgements

This work was supported by the Air Force Office of Scientific Research under grant #F49620-02-1-0211. TEM work was performed in the Materials Research Institute TEM facility at the Pennsylvania State University.

References

1. R. ASHBROOK, *J. Amer. Ceram. Soc.* **60** (1977) 428.
2. Y. WAKU, *Key. Eng. Mat.* **2** (1999) 155.
3. A. SAYIR, S. FARMER, P. DICKERSON and H. YUN, in Proceedings of Material Research Society Symposium (Warrendale, 1995) p. 21.
4. J. Y. PASTOR, P. POZA, J. LORCA, J. I. PENA, R. I. MERINO and V. M. ORERA, *Mater. Sci. Eng.* A **308** (2000) 241.
5. E. C. DICKEY, V. P. DRAVID, P. D. NELLIST, D. J. WALLIS and S. J. PENNYCOOK, *Acta Mater.* **46** (1998) 1801.
6. Y. PADERNO, V. PADERNO, V. FILIPPOV, Y. MIL'MAN and A. MARTYNENKO, *Sov. Powd. Met.* **31** (1992) 700.
7. C. CHEN, W. ZHOU, L. ZHANG, Z. HAO, Y. JIANG and S. YANG, *Compos. Sci. Technol.* **61** (2001) 971.
8. Y. PADERNO, V. PADERNO and V. FILIPPOV, *Jpn. J. Appl. Phys.* **Ser.10** (1994) 190.
9. C. CHEN, W. ZHOU and L. ZHANG, *Prog. Nat. Sci.* **8** (1998) 74.
10. G. ANSTIS, P. CHANTIKUL, B. LAWN and D. MARSHALL, *J. Amer. Ceram. Soc.* **64** (1981) 533.
11. D. B. MARSHALL, T. NOMA and A. EVANS, *ibid.* **10** (1982) c175.
12. Y. PADERNO, V. PADERNO and V. FILIPPOV, in Proceedings of Boron Rich Solids, AIP Conference, NY, 1991, p. 561.
13. M. CARRARD, M. GREMAUD, M. ZIMMERMANN and W. KURZ, *Acta Metall. Mater.* **40** (1992) 983.
14. M. GREMAUD, M. CARRARD and W. KURZ, *ibid.* **39** (1991) 1431.
15. C. S. FRAZER, E. C. DICKEY and A. SAYIR, *J. Cryst. Growth* **233** (2001) 187.
16. Y. PADERNO, V. PADERNO and V. FILIPPOV, *J. Alloy. Compd.* **219** (1995) 116.
17. C. CHEN, W. ZHOU and L. ZHANG, *J. Amer. Ceram. Soc.* **81** (1998) 237.
18. B. LAWN, "Fracture of Brittle Solids" (Cambridge University Press, NewYork, 1993) p. 78.
19. Y. PADERNO, V. PADERNO and V. FILIPPOV, "Advanced Multilayered and Fibre-Reinforced Composites" (Kluwer Academic Publishers, Netherlands, 1998) p. 353.

Received 6 November 2003
and accepted 19 April 2004